



ORIGINAL ARTICLE

Francesco dell’Isola · Pierre Seppecher · Jean Jacques Alibert · Tomasz Lekszycki · Roman Grygoruk · Marek Pawlikowski · David Steigmann · Ivan Giorgio · Ugo Andreaus · Emilio Turco · Maciej Gołaszewski · Nicola Rizzi · Claude Boutin · Victor A. Eremeyev · Anil Misra · Luca Placidi · Emilio Barchiesi  · Leopoldo Greco · Massimo Cuomo · Antonio Cazzani · Alessandro Della Corte · Antonio Battista · Daria Scerrato · Inna Zurba Eremeeva · Yosra Rahali · Jean-François Ganghoffer · Wolfgang Müller · Gregor Ganzosch · Mario Spagnuolo · Aron Pfaff · Katarzyna Barcz · Klaus Hoshcke · Jan Neggiers · François Hild

Pantographic metamaterials: an example of mathematically driven design and of its technological challenges

Received: 9 March 2018 / Accepted: 21 May 2018 / Published online: 30 June 2018
© Springer-Verlag GmbH Germany, part of Springer Nature 2018

Abstract In this paper, we account for the research efforts that have been started, for some among us, already since 2003, and aimed to the design of a class of exotic architected, optimized (meta) materials. At the first stage of these efforts, as it often happens, the research was based on the results of mathematical investigations. The problem to be solved was stated as follows: determine the material (micro)structure governed by those equations that specify a desired behavior. Addressing this problem has led to the synthesis of second gradient materials. In the second stage, it has been necessary to develop numerical integration schemes and

Communicated by Andreas Öchsner.

F. dell’Isola · U. Andreaus · E. Barchiesi (✉)
Dipartimento di Ingegneria Strutturale e Geotecnica, Università degli Studi di Roma “La Sapienza”, Via Eudossiana 18,
00184 Rome, Italy
E-mail: barchiesiemilio@gmail.com

F. dell’Isola · P. Seppecher · T. Lekszycki · I. Giorgio · E. Turco · V. A. Eremeyev · A. Misra · L. Placidi · E. Barchiesi ·
L. Greco · M. Cuomo · A. D. Corte · A. Battista · D. Scerrato · I. Z. Eremeeva · J.-F. Ganghoffer
International Research Center M&MoCS, Università degli Studi dell’Aquila, Via Giovanni Gronchi 18 - Zona industriale di Pile,
67100 L’Aquila, Italy

F. dell’Isola · A. D. Corte
Dipartimento di Ingegneria Civile, Edile-Architettura e Ambientale, Università degli Studi dell’Aquila, Via Giovanni Gronchi
18 - Zona industriale di Pile, 67100 L’Aquila, Italy

F. dell’Isola · I. Giorgio · L. Placidi · E. Barchiesi · A. D. Corte · A. Battista · D. Scerrato · M. Spagnuolo
Research Institute for Mechanics, National Research Lobachevsky State University of Nizhni Novgorod, Nizhny Novgorod,
Russia

P. Seppecher · J. J. Alibert
Institut de Mathématiques de Toulon, Université de Toulon et du Var, Avenue de l’ Université, BP 132, 83957 La Garde Cedex,
France

T. Lekszycki · R. Grygoruk · M. Pawlikowski · M. Gołaszewski · K. Barcz
Institute of Mechanics and Printing, Warsaw University of Technology, 85 Narbutta Street, 02-524 Warsaw, Poland

T. Lekszycki
Department of Experimental Physiology and Pathophysiology, Medical University of Warsaw, 1b Banacha Street, 02-097
Warsaw, Poland

the corresponding codes for solving, in physically relevant cases, the chosen equations. Finally, it has been necessary to physically construct the theoretically synthesized microstructures. This has been possible by means of the recent developments in rapid prototyping technologies, which allow for the fabrication of some complex (micro)structures considered, up to now, to be simply some mathematical dreams. We show here a panorama of the results of our efforts (1) in designing pantographic metamaterials, (2) in exploiting the modern

D. Steigmann

Department of Mechanical Engineering, University of California at Berkeley, 6133 Etcheverry Hall, Mailstop 1740, Berkeley, CA, USA

E. Turco

Dipartimento di Architettura, Design, Urbanistica, Università degli Studi di Sassari, Asilo Sella, Via Garibaldi 35 (1 piano), 07041 Alghero, SS, Italy

N. Rizzi

Dipartimento di Architettura, Università degli studi Roma Tre, Via della Madonna dei Monti 40, 00184 Rome, Italy

C. Boutin

Ecole Nationale des Travaux Publics de l'Etat, LGCB CNRS 5513 - CeLyA, Université de Lyon, 69518 Vaulx-en-Velin Cedex, France

V. A. Eremeyev

Faculty of Civil and Environmental Engineering, Gdańsk University of Technology, ul. Gabriela Narutowicza 11/12, 80-233 Gdańsk, Poland

V. A. Eremeyev

Mathematics, Mechanics and Computer Science Department, South Federal University, Milchakova, str., 8a, Rostov-on-Don, Russia 344090

A. Misra

Civil, Environmental and Architectural Engineering Department, The University of Kansas, 1530 W. 15th Street, Lawrence, KS 66045-7609, USA

L. Placidi

Engineering Faculty, International Telematic University Uninettuno, C.so Vittorio Emanuele II 39, 00186 Rome, Italy

L. Greco · M. Cuomo

Dipartimento di Ingegneria Civile ed Ambientale (sezione di Ingegneria Strutturale), Università di Catania, Edificio Polifunzionale, IV piano, Viale Andrea Doria, 6 I, 95125 Catania, Italy

A. Cazzani

Dipartimento di Ingegneria Civile, Ambientale e Architettura, Università degli studi di Cagliari, Via Marengo 2, Cagliari, Italy

A. Battista

Laboratoire des Sciences de l'Ingénieur pour l'Environnement, Université de La Rochelle, 23 avenue Albert Einstein, BP 33060, 17031 La Rochelle, Italy

Y. Rahali · J.-F. Ganghoffer

Laboratoire d'Energétique et de Mécanique Théorique et Appliquée, University of Lorraine, 2 Avenue de la Forêt de Haye, BP 90161, 54505 Vandoeuvre-lès-Nancy cedex, France

W. Müller · G. Ganzosch

Faculty of Mechanics, Berlin University of Technology, Einsteinufer 5, 10587 Berlin, Germany

M. Spagnuolo

Laboratoire des Sciences des Procédés et des Matériaux, Université Paris 13, Campus de Villetaneuse 99 avenue Jean-baptiste Clément, 93430 Villetaneuse, France

A. Pfaff · K. Hoschke

Fraunhofer Institute for High-Speed Dynamics, Ernst-Mach-Institut, Eckerstraße 4, 79104 Freiburg, Germany

technology of rapid prototyping, and (3) in the mechanical testing of many real prototypes. Among the key findings that have been obtained, there are the following ones: pantographic metamaterials (1) undergo very large deformations while remaining in the elastic regime, (2) are very tough in resisting to damage phenomena, (3) exhibit robust macroscopic mechanical behavior with respect to minor changes in their microstructure and micromechanical properties, (4) have superior strength to weight ratio, (5) have predictable damage behavior, and (6) possess physical properties that are critically dictated by their geometry at the microlevel.

Keywords Pantographic fabrics · Metamaterials · Scientific design · Higher gradient materials

Introduction

Like every other human activity, the design, manufacturing and testing of prototypes of novel materials having a complex and purpose-tailored (micro)structure need the organized efforts of many specialists having a large scope of competence. Therefore, the present work needed the collaboration of many scientists, each one with his/her own specific competences. The order of the authors of this paper has been formed with a simple criterion: it is related to the length of the time period that has seen their involvement in the described joint research efforts and, therefore, does not express any evaluation of the importance of each contribution.

Let us note that, in this paper, no specific length scale is attached to the word “micro.” Specifically, with its use it is meant that at one or at multiple smaller (with respect to the unique macroscale corresponding to that at which phenomena are observed) length scales the material is made of complex microstructures: they consist in the organization of the distribution of matter and its (possibly varying) physical properties.

The aim of this paper is to account, in a unique panoramic view, for the research efforts that we have started (at least the first ones among us) since 2003 and that has produced, in our opinion, some interesting results. The aim of the investigations was more specifically (1) to design novel and exotic architected metamaterials based on a mathematical understanding of the related mechanical problems and on suitably designed numerical simulations, (2) to build the designed prototypes by using 3D printing technology, (3) to test with sensitive apparatuses the so-built prototypes, (4) to elaborate the obtained data with modern image correlation techniques, (5) to produce a careful model fitting of the experimental data by means of the systematic use of numerical simulations, and (6) to compare the proposed models with experimental evidence.

At the first stage of the research effort, as it often happens, the problem was approached from a theoretical point of view. The mathematical models, which were initially introduced, belong to the class of generalized continua: the introduced independent kinematic fields include not only the displacement field but, eventually, also microstretch and/or microrotation fields. The particular class of second gradient continua was more specifically considered: in these media, the strain energy depends on the displacement gradient and on its second gradient. The reasons of their name are therefore clear: in second gradient continua the strain energy may depend on the second gradient of displacement. Second gradient continua can be regarded as media endowed with a tensorial microstructure in which a constraint is applied, namely it requires that the microstructure tensor is equal to the placement gradient. The problem to be solved was: given a desired behavior, to find at first the evolution equations modeling such a behavior and then to characterize the material (micro)structure governed by the chosen equations.

In the second stage, it was necessary to develop numerical integration schemes and the corresponding codes for solving, in physically relevant cases, the equations chosen to describe the desired behavior. Finally, it was necessary to build the microstructures. This was possible by means of the recent developments of rapid prototyping technologies, which allow for the fabrication of those which, up to now, were simply mathematical dreams.

In this paper, we show the results of our efforts in designing pantographic metamaterials, in the mechanical testing of real prototypes, and evidence is provided on their exotic behavior. With the latest advancements (e.g., 3D-printing technology and, more generally, of rapid prototyping techniques), the small-scale production of materials with complex geometries has become more affordable than ever [1–4]. The exploitation of these new technologies has made possible the development in the last few years of materials with very different substructures.

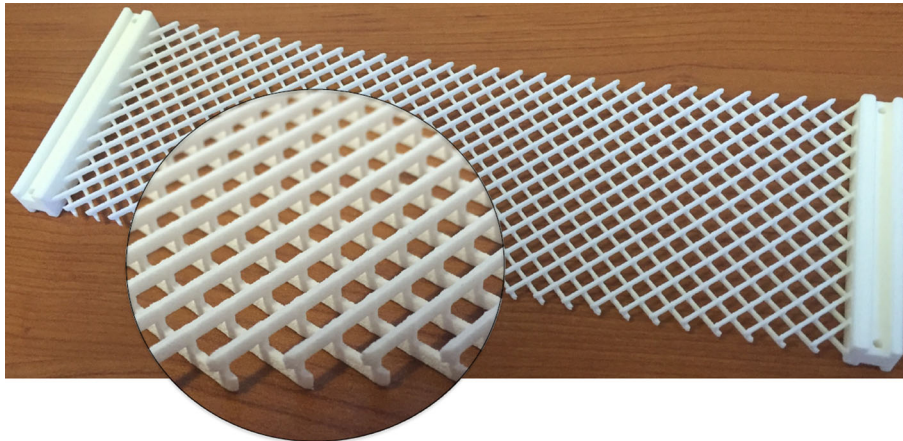


Fig. 1 Example of pantographic structure [13]

One of the research goals whose achievement has been sped up by rapid prototyping is to determine and study new microstructures that, at a well-specified macroscopic scale, exhibit a behavior that can be described by nonstandard mathematical models like generalized continuum theories. Many of these theories, that today are being called “generalized” (as opposed to “classical” theories), were formulated before or together with so-called “classical” theories and then lost [5,6]. It is possible to state that some of these theories were already known at least two centuries ago [7,8]. Pantographic structures (Fig. 1) have been proposed as a metamaterial [9], which is well described by second gradient continuum theories [10–12].

1 Modeling and experiments in elastic regime

The theoretical interest in pantographic structures derives from the fact that, in order to describe their exotic phenomenology, one has to utilize higher gradient continuum theories [14,15] or micromorphic theories [16,17] with the related problem of homogenization [18] and of different strategies for numerical integration [19,20].

1.1 Homogenization of periodic truss modular structures

Throughout the history of mechanics, several multiscale procedures have been developed in order to relate macromodels with micromodels, the first attempts tracing back to Maxwell and Saint-Venant [21]. An approach that has proven to be effective is based on the postulate of a macroscopic and a microscopic model and of a kinematic correspondence between the deformations defined within the two models. Successively, it is postulated that the power expended in corresponding motions coincides. In this way, it is possible to obtain the coefficients of the constitutive equations of the macromodel in terms of properties of the building blocks constituting the microscopic model. The macromodel is not the result of the homogenization process but is, instead, assumed a priori. Formal asymptotic expansion can help to encompass this difficulty, and a microscopic model made up of linear Euler beams leads to a simple macroscopic second gradient model of a 1D planar beam [11].

The structure that is considered at the microlevel is the so-called pantographic structure (Fig. 2). It is assumed that the considered pantographic microstructure is made up of a very large number of small modules and the limit behavior when such a number tends to infinity, i.e., the homogenized macromodel, is studied. Using Gamma-convergence technique, it is proven that the homogenized model is the postulated second gradient model [11]. Successively, a modified (Warren-type) pantographic structure is proposed as micromodel in order to get for the first time a third gradient planar beam model (Fig. 3), whose general properties were already studied by Mindlin and Tiersten [22], and Dillon and Perzyna [23]. Such structures possess other floppy modes (i.e., placements for which the strain energy vanishes) than, trivially, rigid motions. The pantographic beam does not store any energy when undergoing uniform extension, while the Warren-type pantographic beam does not store any energy when undergoing uniform flexure.

In Ref. [24], formal asymptotic expansion procedures, already employed [11,13], are systematically considered in the framework of linear elasticity in order to determine the effective behavior of periodic structures

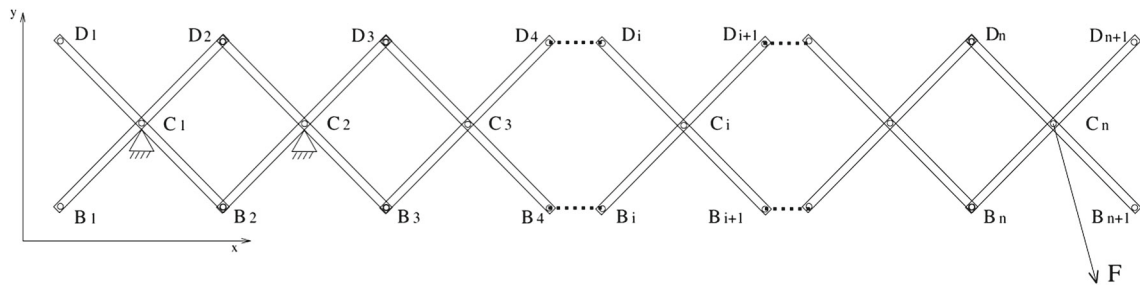


Fig. 2 Pantographic microstructure considered in Ref. [11]

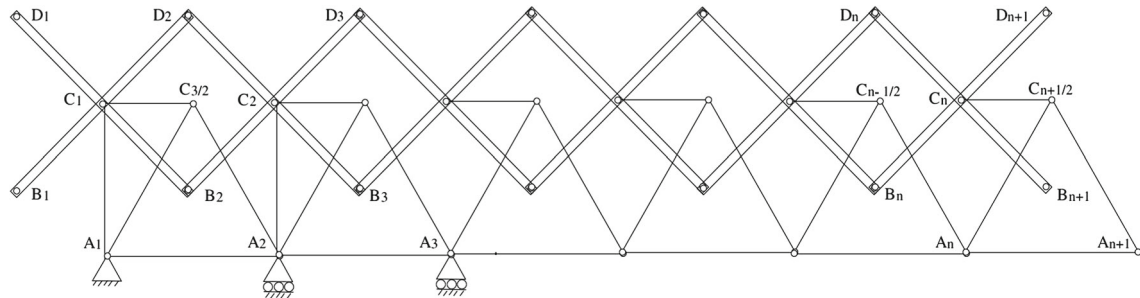


Fig. 3 Warren-type pantographic microstructure [11]

made of welded elastic bars. Noting that flexural and torsional stiffnesses of isotropic homogeneous elastic bars are much smaller than the extensional one entails an asymptotic rescaling of stiffnesses giving rise to interesting macromodels. In Ref. [24], different examples of two-dimensional or three-dimensional microstructures that lead to generalized 1D, 2D or 3D continua like Timoshenko beam, Mindlin-Reissner plate, strain gradient, Cosserat, or micromorphic continua are provided.

Reference [25], in the spirit of pantographic fabrics, addresses one of the main challenges in the modern theory of materials: the determination of those microstructures that produce, at the macrolevel, a class of metamaterials whose elastic range is many orders of magnitude wider than the one exhibited by “conventional” materials. With pantographic microstructures, which are made of “long” microbeams, it is possible to obtain metamaterials whose elastic range spans up to an elongation exceeding 30%. It is shown that the same behavior can be obtained by means of an internal microstructure based on a king post pattern (Fig. 4). This solution shows many advantages, namely it only involves microbeams; all beams are only undergoing extension or contraction; all internal constraints are terminal pivots. While the elastic strain energy can be determined as easily as in the case of a long-beam microstructure, the proposed design seems to have remarkable advantages: it seems to be more damage resistant and, therefore, to be able to have a wider elastic range; it can be obtained with the same three-dimensional printing technology; it seems to be less subject to compression buckling. The following analyses were carried out: (1) the derivation of Hencky-type discrete models for king post trusses, (2) the application of an effective integration scheme to a class of relevant deformation tests for the proposed metamaterial, and (3) the numerical determination of an equivalent second gradient continuum model.

1.2 Pipkin elastic plate model with inextensible fibers

Starting from a number of papers by Pipkin et al. [26–33], 2D continua consisting of two orthogonal families of inextensible fibers were considered [34] and an adaptation to the case of pantographic structures has been presented [10,35]. First, a 2D continuum, whose reference shape is given by the rectangular domain $\Omega \subset \mathbb{R}^2$ with the tallest side three times longer than the shorter one, has been considered. Considering only planar motions, the current shape of Ω is described by the suitably regular macro-placement $\chi : \Omega \rightarrow \mathbb{R}^2$, with $(X_1, X_2) \mapsto^{\chi} (x_1, x_2)$. An orthogonal frame of reference $(\mathcal{O}, \xi_1, \xi_2)$, whose orientation is the same of the inextensible fibers in the reference configuration and whose coordinates are dimensionless, is introduced. Accordingly, we have

$$\xi_1 := \frac{1}{l}(X_1 - X_2) + \frac{1}{2}, \quad \xi_2 := \frac{1}{l}(X_1 + X_2) + \frac{1}{2}. \tag{1}$$

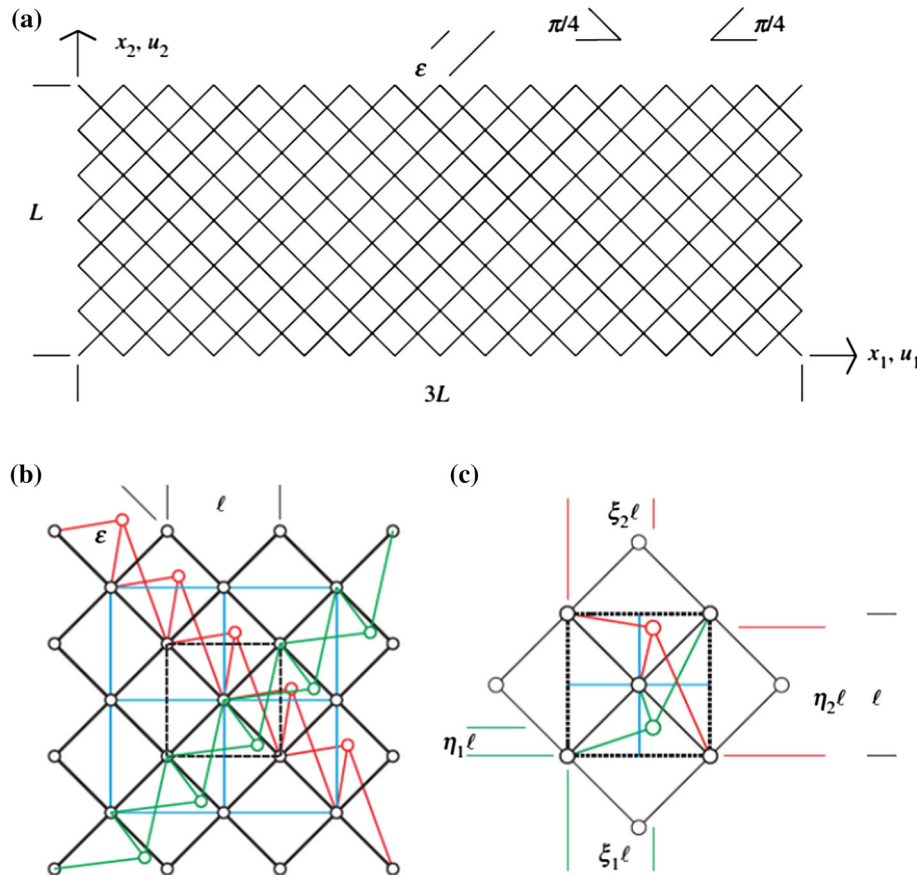


Fig. 4 King post pantographic lattice: geometry (a), pantographic rods (in black), king post rods (in red and green), auxiliary rods (in cyan) (b), and king post geometric parameters (c) (color figure online)

A graphical depiction of the introduced quantities is given in Fig. 5. A pair (D_1, D_2) of orthonormal vectors, the basis associated with the frame of reference $(\mathcal{O}, \xi_1, \xi_2)$, is further introduced. The two vectors D_1 and D_2 are tangent to the two families of fibers in the reference configuration. The inextensibility constraint can be encoded in the following way. A curve β is inextensible for a placement χ if, for every part α of β , $\chi(\alpha)$ has the same length of α .

By definition d_1 and d_2 are considered to be the push-forward vectors, in the current configuration, of the vectors D_1 and D_2 , respectively, i.e., $d_\alpha = FD_\alpha$, $\alpha = 1, 2$, where $F = \nabla \chi$. The inextensibility constraint implies that $\|d_1(\xi_1, \xi_2)\| = \|d_2(\xi_1, \xi_2)\| = 1$ for all (ξ_1, ξ_2) such that χ is locally continuously differentiable. In the celebrated Rivlin paper [36], it is stated that when χ is twice continuously differentiable on an open simply linearly connected subset Δ of Ω , the fiber inextensibility assumption allows the following representation formula

$$\chi^\Delta(\xi_1, \xi_2) = \chi_1^\Delta(\xi_1) + \chi_2^\Delta(\xi_2) \tag{2}$$

to be found for the restriction to Δ of the placement. If $\mu_1^\Delta(\xi_1)$ and $\nu_1^\Delta(\xi_1)$ denote the projections of $\chi_1^\Delta(\xi_1)$ on D_1 and D_2 , respectively, and $\nu_2^\Delta(\xi_2)$ and $\mu_2^\Delta(\xi_2)$ the projections of $\chi_2^\Delta(\xi_2)$ on D_1 and D_2 , respectively, then

$$\chi_1^\Delta(\xi_1) = \mu_1^\Delta(\xi_1)D_1 + \nu_1^\Delta(\xi_1)D_2 \quad \text{and} \quad \chi_2^\Delta(\xi_2) = \nu_2^\Delta(\xi_2)D_1 + \mu_2^\Delta(\xi_2)D_2 \tag{3}$$

The map χ is assumed to be piecewise twice continuously differentiable. It is worth noting that the matrix representation of F on the subset Δ and for the reference frame defined by D_1 and D_2 is expressed as

$$[F^\Delta]_{(D_1, D_2)} = \begin{bmatrix} \mu_{1,1}^\Delta(\xi_1) & \nu_{2,2}^\Delta(\xi_2) \\ \nu_{1,1}^\Delta(\xi_1) & \mu_{2,2}^\Delta(\xi_2) \end{bmatrix} \tag{4}$$

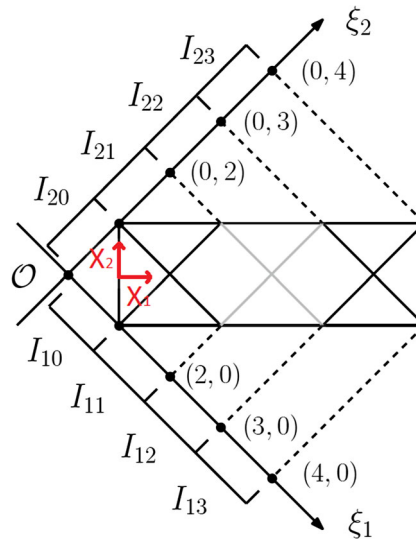


Fig. 5 Material (Lagrangian) coordinates adapted to inextensible fiber configuration [10]

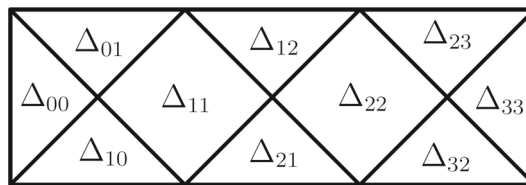


Fig. 6 Domain pattern induced by the boundary conditions [10]

and that the functions $\chi_\alpha^\Delta(\xi_\alpha)$ ($\alpha = 1, 2$) are determined up to two scalar constants C_1 and C_2 , i.e., if the decomposition (2) holds with the representation (3), then the following alternative representation holds

$$\begin{aligned} \chi_1^\Delta(\xi_1) &= (\mu_1^\Delta(\xi_1) + C_1) D_1 + (v_1^\Delta(\xi_1) + C_2) D_2 \\ \chi_2^\Delta(\xi_2) &= (v_2^\Delta(\xi_2) - C_1) D_1 + (\mu_2^\Delta(\xi_2) - C_2) D_2 \end{aligned} \tag{5}$$

The inextensibility constraint, together with the assumption that the map χ be piecewise C^2 , implies that there exist two quantities $\vartheta_1^\Delta(\xi_1)$ and $\vartheta_2^\Delta(\xi_2)$ such that

$$d_1^\Delta = \cos \vartheta_1(\xi_1) D_1 + \sin \vartheta_1(\xi_1) D_2 \quad \text{and} \quad d_2^\Delta = \sin \vartheta_2(\xi_2) D_1 + \cos \vartheta_2(\xi_2) D_2 \tag{6}$$

The above statement stands since d_1^Δ and d_2^Δ belong to $S_2 = \{x \in \mathbb{R}^2 : \|x\| = 1\}$.

Let Σ_1 and Σ_2 denote the left and right short sides, respectively, of the boundary $\partial\Omega$ of Ω . The following boundary conditions are considered:

1. vanishing displacement on Σ_1 ;
2. nonvanishing displacement u_0 on Σ_2 .

Because of fiber inextensibility, the boundary conditions on Σ_1 and Σ_2 determine the placement field not just at the boundary, but also in some regions of the interior of Ω [34], i.e., on the regions Δ_{00} and Δ_{33} of Fig. 6.

Hence, the space of admissible placements for the Pipkin continuum under study is uniquely determined by the continuous piecewise twice continuously differentiable fields $\mu_1(\xi_1)$ and $\mu_2(\xi_2)$. In particular, given the boundary conditions i.e., $\mu(\xi)$ is known on Δ_{00} and Δ_{33} (for $\xi_\alpha \in [0, 1] \cup [3, 4]$), we are interested in determining $\mu_\alpha(\xi_\alpha)$ only for $\xi_\alpha \in [1, 3]$. By looking at the ordinary differential equations

$$\frac{d\mu_\alpha(\xi_\alpha)}{d\xi_\alpha} = \cos \vartheta_\alpha(\xi), \quad \alpha = 1, 2 \tag{7}$$

which derive from Eqs. (5) and (6). Providing an integration constant through the continuity condition $\mu_\alpha(1) = 1$ at point (1, 1) uniquely defines the space of admissible placements for the Pipkin continuum by means of the fields $\vartheta_1(\xi_1)$ and $\vartheta_2(\xi_2)$.

In fiber-inextensible 2D Pipkin continua, it is customary to introduce the *shear deformation* γ as a strain measure. The shear deformation is defined as the scalar product of the fiber directions in the deformed configuration and, reminding the inextensibility assumption and Eq. (6), reads

$$\gamma(\xi_1, \xi_2) := d_1 \cdot d_2 = \cos\left(\frac{\pi}{2} - \vartheta_1(\xi_1) - \vartheta_2(\xi_2)\right) = \sin(\vartheta_1(\xi_1) + \vartheta_2(\xi_2)) \quad (8)$$

The following kinematic constraint should be enforced

$$-\frac{\pi}{2} < \vartheta_1 + \vartheta_2 < \frac{\pi}{2} \quad (\implies -1 < \gamma < 1) \quad (9)$$

if the case $\vartheta_1 + \vartheta_2 = \pm\frac{\pi}{2}$, which stands for overlapping fibers is to be avoided. Now that the space of fields $\vartheta_1(\xi_1)$ and $\vartheta_2(\xi_2)$ uniquely describes admissible placements, the strain energy density $W(\vartheta_1, \vartheta_2, \frac{d\vartheta_1}{d\xi_1}, \frac{d\vartheta_2}{d\xi_2})$ is introduced. It is assumed to have the form

$$W\left(\vartheta_1, \vartheta_2, \frac{d\vartheta_1}{d\xi_1}, \frac{d\vartheta_2}{d\xi_2}\right) = \alpha g(f(\gamma)) + \beta g(\|\nabla f(\gamma)\|) \quad (10)$$

with $g(x) = \frac{1}{2}x^2$. Different functions f have been studied [10, 35], among which:

- S $f(\gamma) = \gamma$
- Q $f(\gamma) = \arcsin \gamma$
- T $f(\gamma) = \tan(\arcsin \gamma)$

Henceforth the case $\alpha = 1, \beta = 0$ is referred to as *first gradient* (1g), and $\alpha = 0, \beta = 1$ as *second gradient* (2g). Numerical results [37–41] show that the final configurations obtained by using second gradient energies are smoother than those with the first gradient approach. In the following, numerical results will be reported for standard bias extension, shear and rotation tests, which confirm such a statement. Among all experiment, the bias test has been extensively analyzed. In a standard bias extension test, $u_{01} = u_{02} := u_0$. Then, a new property has to be enforced on the placement function χ , which holds true for the bias extension test, while not, e.g., for the shear tests that will be considered later on. Only placements functions that are symmetric with respect to the X_1 axis can be considered. With regard to the reference frame $(\mathcal{O}, \xi_1, \xi_2)$, this means that given a point P of coordinates (ξ, η) and its symmetric (with respect to X_1) P_S whose coordinates are (η, ξ) , the conditions

$$d_1(P) \cdot D_\alpha = d_2(P_S) \cdot D_{3-\alpha} \quad \alpha = 1, 2 \quad (11)$$

must be satisfied. They imply that $v_{1,1}(\xi) = v_{2,2}(\xi)$ and $\mu_{1,1}(\xi) = \mu_{2,2}(\xi)$ and in turn, given the boundary conditions, $v_1(\xi) = v_2(\xi) := v(\xi)$ and $\mu_1(\xi) = \mu_2(\xi) := \mu(\xi)$. It is thus possible to state that in a standard bias test the space of admissible placements for the Pipkin continuum is uniquely determined by the (globally continuous) piecewise twice continuously differentiable field $\mu(\xi)$. Since $\mu(\xi)$ is known on Δ_{00} and Δ_{33} , i.e., for $\xi \in [0, 1] \cup [3, 4]$, we are interested in determining $\mu(\xi)$ only for $\xi \in [1, 3]$. By analyzing ordinary differential equations

$$\frac{d\mu_\alpha(\xi)}{d\xi} = \cos \vartheta_\alpha(\xi), \quad \alpha = 1, 2 \quad (12)$$

it is concluded that $\vartheta_1(\xi) = \vartheta_2(\xi) := \vartheta(\xi)$ with $\vartheta(\xi)$ a (possibly discontinuous) piecewise continuously differentiable field. Numerical results are shown in Figs. 7 and 8. Figure 7 provides a general overview of the qualitative differences among different choices of α, β and of the function f in Eq. (10). In Fig. 8, a comparison between final shapes of the rectangular sample is reported when modeled with 1gT and 2gT strain energy densities. It is noteworthy that the final shapes are much smoother when a second gradient model is employed, as strong variations of the field variable are penalized in the energy.

Let us now turn to reporting shear tests. Thus, the symmetry assumptions, which were previously introduced when dealing with the standard bias extension test, are no longer considered. When modeling the shear test, the condition $u_{01} = -u_{02}$ holds. The results are shown in Figs. 9 and 10. In particular, Fig. 9 gives an overview of the qualitative differences among different choices of α, β and of the function f defined in Eq. (10). The non-monotonicity of the 1gS and 2gS models is not physically grounded. Besides, in Fig. 10 comparisons between final shapes of the rectangular samples, modeled with 1gT and 2gT strain energy density, are reported. Again, the final shapes are much smoother when a second gradient model is employed.

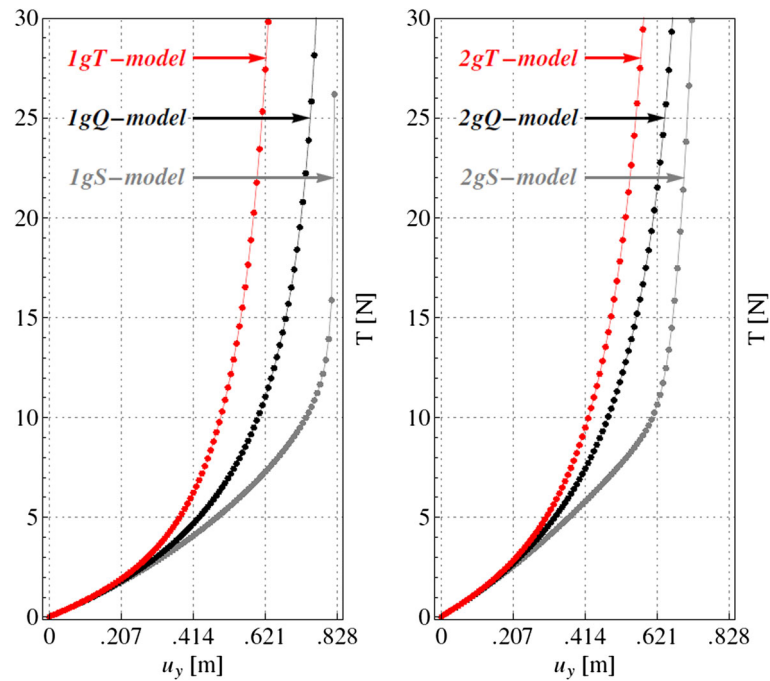


Fig. 7 Bias extension test. Resultant (normal) forces on the short side (computed by means of Castigliano’s first theorem) versus vertical component of prescribed displacement: **a** first gradient energy models, **b** second gradient energy models

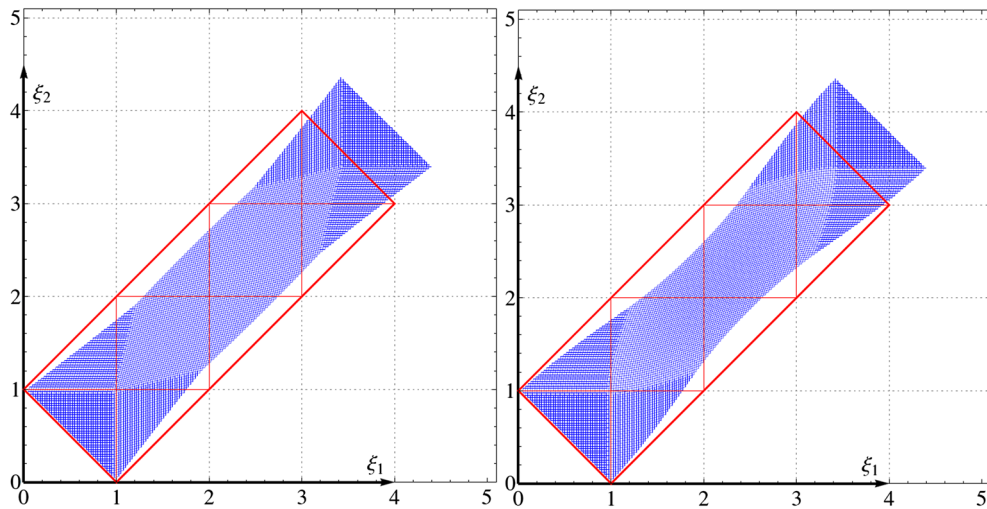


Fig. 8 Bias extension test. Reference and deformed configurations for the first gradient 1gT (left) and second gradient 2gT (right) models

1.3 Discrete Hencky-type elastic plate model

A discrete approach has been introduced for pantographic structures [13] and subsequently studied [42,43]. Modeling assumptions for the micromodel are based on physically grounded considerations about the real microstructure of pantographic sheets and apply to the case of large deformations. In particular, trying to comply with reported experimental evidences [10,13], the extension of fibers is accounted for by connecting adjacent material particles with extensional springs. Moreover, at each node of the lattice, rotational springs, which are deformed when the angle spanned by two contiguous extensional springs is changed, are introduced. To account for the fact that such materials show two privileged material directions, a Lagrangian Cartesian orthonormal coordinate system is introduced. Its associated basis of unit vectors is (D_1, D_2) made of two

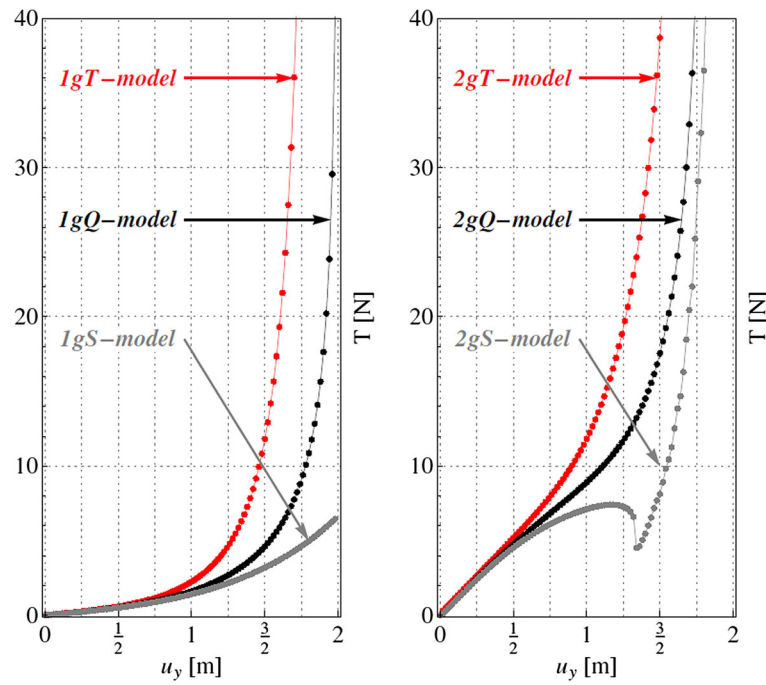


Fig. 9 Shear test. Resultant (shear) forces on the short side (computed by means of Castigliano’s first theorem) versus vertical component of prescribed displacement: **a** first gradient energy models, **b** second gradient energy models

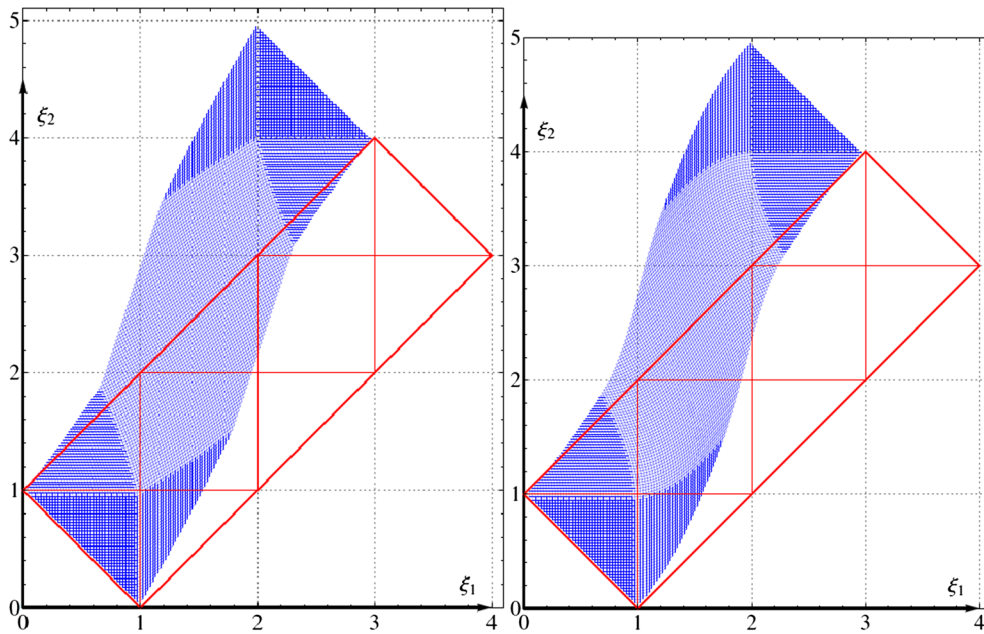


Fig. 10 Shear test. Reference and deformed configurations for the first gradient $1gT$ (left) and second gradient $2gT$ (right) models

orthonormal vectors that represent the directions of the families of fibers constituting the pantographic structure in the reference configuration. In such configuration, the lattice body points are located at the positions

$$P_{i,j} = (i\epsilon, j\epsilon), \quad i = 0, 1, \dots, N \text{ and } j = 0, 1, \dots, M \tag{13}$$

and $p_{i,j}$ denotes the current configuration position of the body point placed at $P_{i,j}$ in the reference configuration. The body points at the nodes $P_{i,j}$ are connected by extensional springs along each one of the coordinate lines

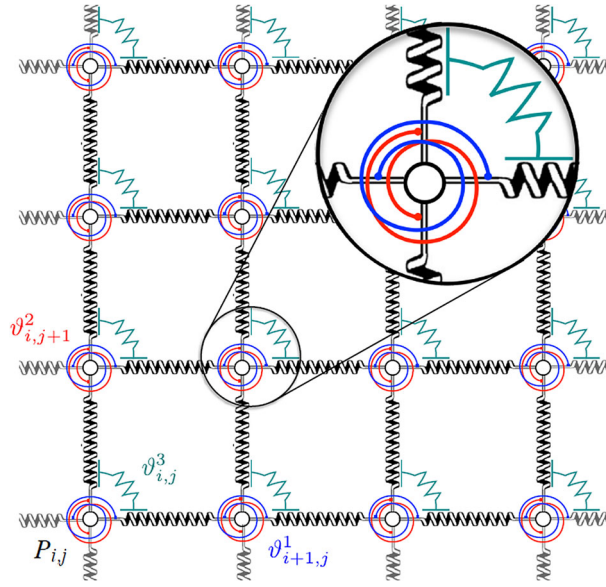


Fig. 11 Micromodel of a pantographic sheet with a detail of the three rotational springs [13]

(Fig. 11) and their deformation energies depend on the distances between adjacent contiguous points in the current configuration, i.e., on the distance between $p_{i,j}$ and $p_{i,j+1}$ for the fibers parallel to D_1 in the reference configuration, and on the distance between $p_{i,j}$ and $p_{i+1,j}$ for the fibers parallel to D_2 in the reference configuration. The first type of extensional spring is characterized by the rigidity $k_{i,j}^1$ and the second kind by $k_{i,j}^2$. Such extensional rigidities are related to the extensional behavior, respectively, of the two families of fibers. As mentioned before, at each node there are also three rotational springs whose deformation energies depend, respectively, on the angles:

1. $\vartheta_{i,j}^1$ formed by the vectors $p_{i-1,j} - p_{i,j}$ and $p_{i+1,j} - p_{i,j}$,
2. $\vartheta_{i,j}^2$ formed by the vectors $p_{i,j-1} - p_{i,j}$ and $p_{i,j+1} - p_{i,j}$,
3. $\vartheta_{i,j}^3$ formed by the vectors $p_{i,j+1} - p_{i,j}$ and $p_{i+1,j} - p_{i,j}$.

The postulated strain energy for the microscopic Lagrangian discrete system having its configuration specified by the set of parameters $\{p_{i,j}\}$ reads

$$\begin{aligned}
 U(\{p_{i,j}\}) = & \sum_j \sum_i \frac{k_{i,j}^1}{2} (\|p_{i+1,j} - p_{i,j}\| - \epsilon)^2 + \sum_j \sum_i b_{i,j}^1 (\cos \vartheta_{i,j}^1 + 1) \\
 & + \sum_j \sum_i \frac{k_{i,j}^2}{2} (\|p_{i,j+1} - p_{i,j}\| - \epsilon)^2 + \sum_j \sum_i b_{i,j}^2 (\cos \vartheta_{i,j}^2 + 1) \\
 & + \sum_j \sum_i \frac{b_{i,j}^3}{2} \left| \vartheta_{i,j}^3 - \frac{\pi}{2} \right|^\xi
 \end{aligned} \tag{14}$$

On the one hand, the rigidities $b_{i,j}^1$ and $b_{i,j}^2$ are related, respectively, to the bending behavior of the two families of fibers. The rigidities $b_{i,j}^3$, on the other hand, are associated with the torsional stiffness of the pivots connecting the two families of fibers, ξ being a parameter that is equal to 2 for a standard linear case.

In subsequent papers [42,43], the discrete (elastic) quasi-static Hencky-type spring model, made of extensional and rotational (i.e., torsional) springs, is solved at each iteration by energy minimization. Even if the model does not contemplate external forces, it would be very easy to consider the discrete analogous forces leading, after a homogenization like the one presented later on, to external bulk forces and double forces. In Fig. 12, the equilibrium shape resulting from a standard bias extension test simulation using the strain

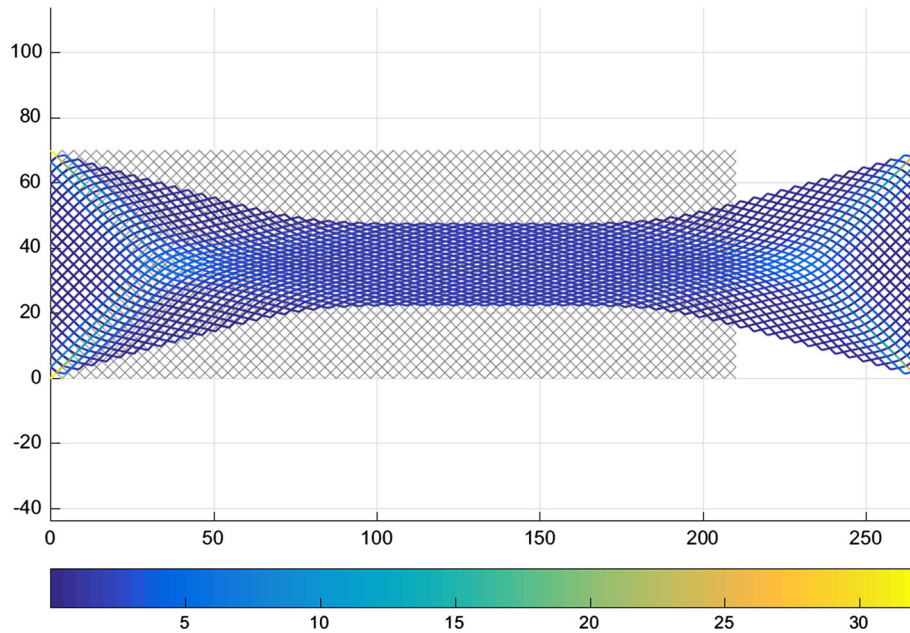


Fig. 12 Bias extension test simulation using the micromodel when $M = 20$ and $N = 60$: reference configuration (gray), current shape and color bar of the internal forces on extensional springs [43] (color figure online)

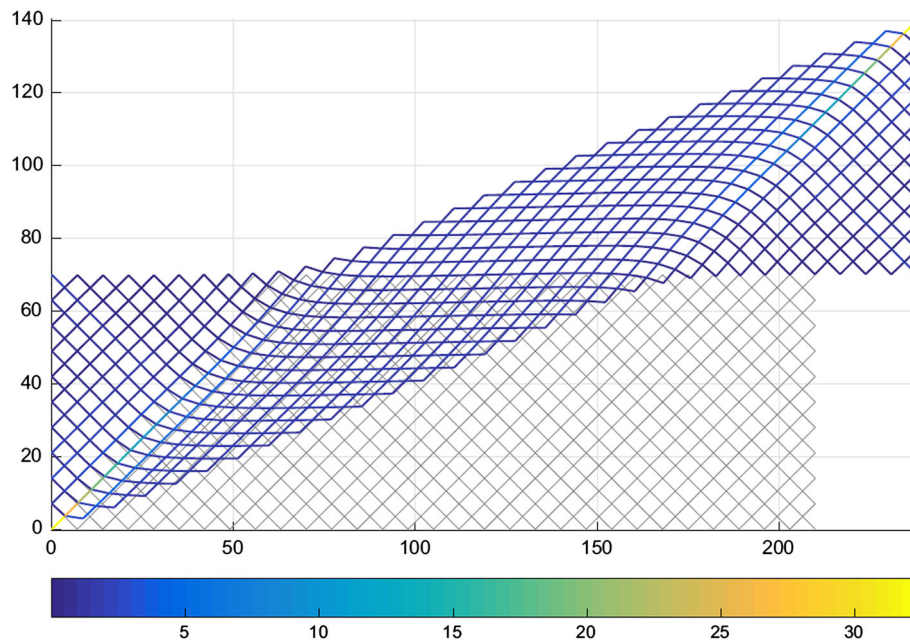


Fig. 13 Shear-extension test simulation using the micromodel: reference configuration (gray), current shape and color bar of the internal forces on extensional springs for $M = 10$ and $N = 30$ [43] (color figure online)

energy (16) is shown, along with colors indicating the magnitude of internal forces on extensional springs computed in the current configuration, and whose expression is given in Ref. [43]. In the same manner, in Fig. 13, the equilibrium shape resulting from a shear test simulation is shown.

1.4 À la Piola homogenized elastic plate model

Considering the discrete Hencky-type micromodel presented above, a 2D continuum macromodel has been derived by means of micro–macro transitions. Expanding in truncated Taylor series the kinematic map [13], the microplacement field of material particles at the nodes of the referential lattice is computed by means of the values, in such nodes, of a regular macro-placement and its first gradient. Such a map determines a unique micromotion once a macro-motion is given. The micro–macro transition is obtained by equating the microstrain energy with the macroscopic counterpart, thus obtaining a macroscopic Lagrangian surface density of strain energy in terms of the constitutive coefficients appearing in the postulated expression of the microstrain energy. Numerical simulations with both discrete and homogenized models show that the homogenized model is representative of the microscopic response [42,43]. Following the notation introduced above, we now consider a 2D continuum whose reference shape is given by a rectangular domain $\Omega = [0, N\epsilon] \times [0, M\epsilon] \subset \mathbb{R}^2$. Very often, it is assumed that $N = 3M$, which is the standard relation between the width and height of a fabric specimen for experimental and numerical tests. By assuming planar motions, the current shape of Ω is described by regular macro-placement $\chi : \Omega \rightarrow \mathbb{R}^2$. The kinematic map providing the micro–macro identification is the so-called Piola ansatz and we accordingly choose $p_{i,j} = \chi(P_{i,j}) \quad \forall i = 1, \dots, N, \forall j = 1, \dots, M$. Assuming that $\chi(\cdot)$ is at least twice differentiable at $P_{i,j}$, the following 2nd-order approximations are obtained

$$\begin{aligned} \|p_{i+1,j} - p_{i,j}\| &= \|\chi(P_{i+1,j}) - \chi(P_{i,j})\| \simeq \epsilon \|F(P_{i,j})D_1 + \frac{\epsilon}{2} \nabla F(P_{i,j})|D_1 \otimes D_1\| \\ \|p_{i,j+1} - p_{i,j}\| &= \|\chi(P_{i,j+1}) - \chi(P_{i,j})\| \simeq \epsilon \|F(P_{i,j})D_2 + \frac{\epsilon}{2} \nabla F(P_{i,j})|D_2 \otimes D_2\| \end{aligned} \quad (15)$$

where F is the deformation gradient $\nabla \chi$. The reader is referred to the original papers [13,42,43] for further details. Equation (15) have been used for the homogenization procedure of two addends of Eq. (14). In order to address the other three terms, the cosines of the angles $\vartheta_{i,j}^\alpha$ ($\alpha = 1, 2$) and $\vartheta_{i,j}^3$ are derived as functions of the macro-placement χ . Using analogous Taylor expansions as those in Eq. (15) neglecting $o(\epsilon^2)$ terms, and writing all quantities in terms of the displacement χ , the strain energy of the micromodel becomes

$$\begin{aligned} U(\{p_{i,j}\}) &= \sum_j \sum_i \sum_\alpha \frac{k_{i,j}^\alpha}{2} \epsilon^2 (\|F(P_{i,j})D_\alpha + \frac{\epsilon}{2} \nabla F(P_{i,j})|D_\alpha \otimes D_\alpha\| - 1)^2 \\ &+ \sum_j \sum_i \sum_\alpha b_{i,j}^\alpha \left[\frac{\|\nabla F(P_{i,j})|D_\alpha \otimes D_\alpha\|^2}{\|F_{i,j}D_\alpha\|^2} - \left(\frac{F(P_{i,j})D_\alpha \cdot \nabla F(P_{i,j})|D_\alpha \otimes D_\alpha}{\|F_{i,j}D_\alpha\|^2} \right)^2 \right] \frac{\epsilon^2}{2} \\ &+ \sum_j \sum_i \frac{b_{i,j}^3}{2} \left| \arccos \left(\frac{F(P_{i,j})D_1 \cdot F(P_{i,j})D_2}{\|F(P_{i,j})D_1\| \cdot \|F(P_{i,j})D_2\|} \right) - \frac{\pi}{2} \right|^\xi, \end{aligned} \quad (16)$$

Rescaling the rigidities as

$$k_{i,j}^\alpha = \mathbb{K}_e^\alpha; \quad b_{i,j}^\alpha = \mathbb{K}_b^\alpha; \quad b_{i,j}^3 = \mathbb{K}_p \epsilon^2 \quad (17)$$

and letting $\epsilon \rightarrow 0$, the strain energy of the macroscopic system reduces to

$$\begin{aligned} U(\chi(\cdot)) &= \int_\Omega \sum_\alpha \frac{\mathbb{K}_e^\alpha}{2} \|FD_\alpha - 1\|^2 dS \\ &+ \int_\Omega \sum_\alpha \frac{\mathbb{K}_b^\alpha}{2} \left[\frac{\|\nabla F|D_\alpha \otimes D_\alpha\|^2}{\|FD_\alpha\|^2} - \left(\frac{FD_\alpha \cdot \nabla F|D_\alpha \otimes D_\alpha}{\|FD_\alpha\|^2} \right)^2 \right] dS \\ &+ \int_\Omega \frac{\mathbb{K}_p}{2} \left| \arccos \left(\frac{FD_1 \cdot FD_2}{\|FD_1\| \cdot \|FD_2\|} \right) - \frac{\pi}{2} \right|^\xi dS. \end{aligned} \quad (18)$$

It is noteworthy that the shear strain introduced in the considered macromodel is different from that defined in the Pipkin continuum model [see Eq. (8)]. In Fig. 14, equilibrium shapes and their corresponding shear strains are compared for different (pure) shear test simulations (refer to problem 2 above) using the strain energy (18). Reference [18] has first addressed the homogenization à la Piola of pantographic fabrics in a linear setting, proving that the homogenization of pantographic fabrics gives rise to second gradient continua.

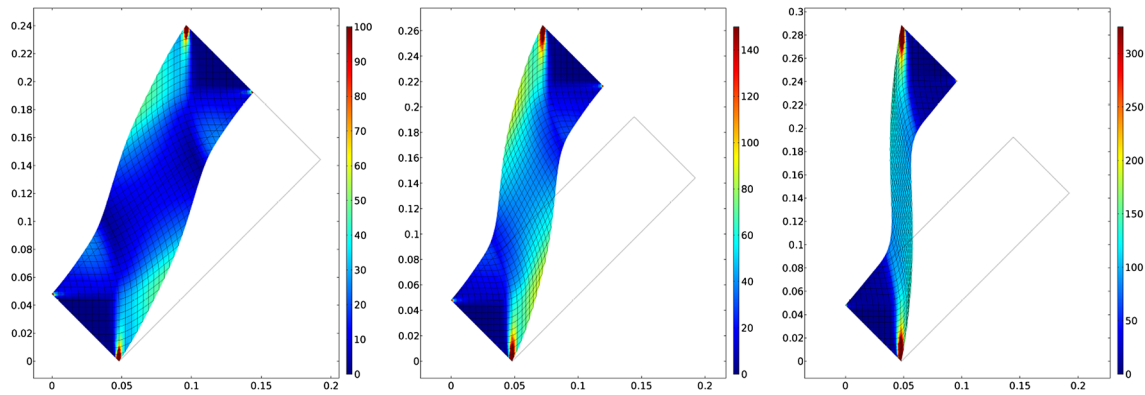


Fig. 14 Equilibrium shape and strain energy density when a shear displacement is prescribed [13] (color figure online)

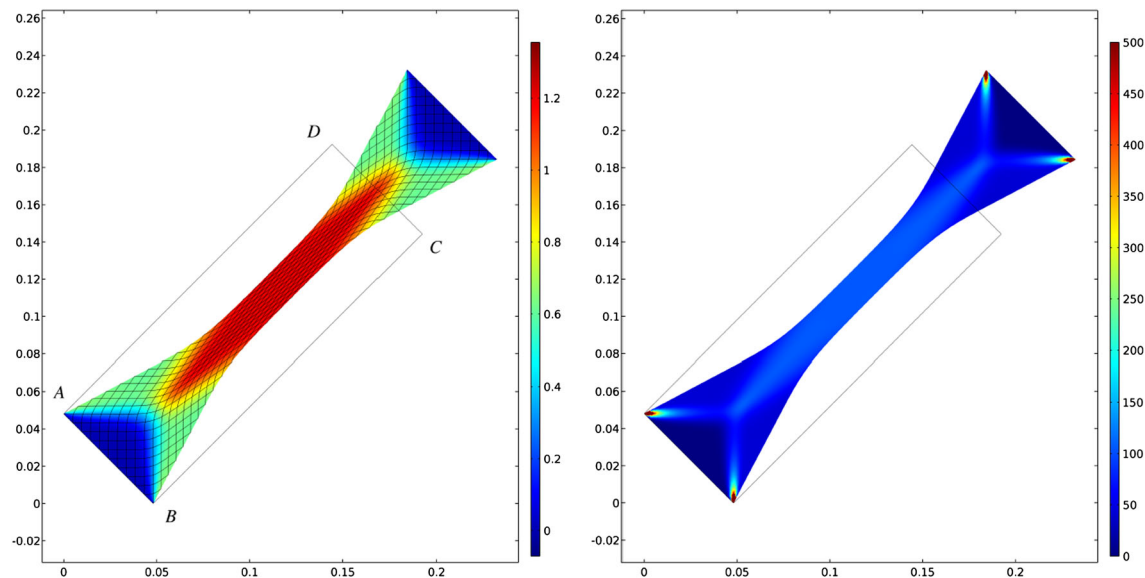


Fig. 15 Numerical simulation of the bias extension test. Colors indicate the shear strain relative to the initial fiber axes (left) and the strain energy density (right) [13]

Several numerical simulations show the presence of (internal) boundary layers, a hallmark of second gradient theories. In Fig. 15, numerical simulations of the bias extension test are shown. The colors indicate the shear strain relative to the initial fiber axes (left) and the strain energy density (right) [13]. In Fig. 16, color maps of the strain energy density are shown for standard bias extension test (left) and combined rotation-compression test (right) of a rectangular linear elastic specimen pantographic fabrics with holes.

The well-posedness of linearized equilibrium equations deriving from the stationarity of the energy functional (18), which is valid in the neighborhood of a stress free configuration for pantographic sheets, cannot be immediately studied by using the results available in the literature. It has been proven that the standard strategy involving the use of Poincaré inequality, Lax–Milgram Theorem, and coercivity of bilinear strain energy form also apply in the context of linear elastic pantographic sheets [44]. The key idea is the exploitation of an unusual energy space, where the solutions relative to well-posed boundary conditions are looked for. It is observed that the energy space of linear pantographic sheets, i.e., the space of functions fulfilling boundary conditions for which the strain energy is meaningful, is included in a special class of Sobolev spaces, the so-called Anisotropic Sobolev Space. The definition of Anisotropic Sobolev Space was conceived on purely logical grounds by Sergei M. Nikol'skii and has to be used in order to apply the abstract Hilbertian setting of solution strategy. Thus, in order to address the well-posedness of the planar linearized equilibrium problem for homogenized pantographic lattices, (1) a class of subsets of anisotropic Sobolev space is introduced as the most suitable energy space relative to assigned boundary conditions; (2) it is proved that the considered strain

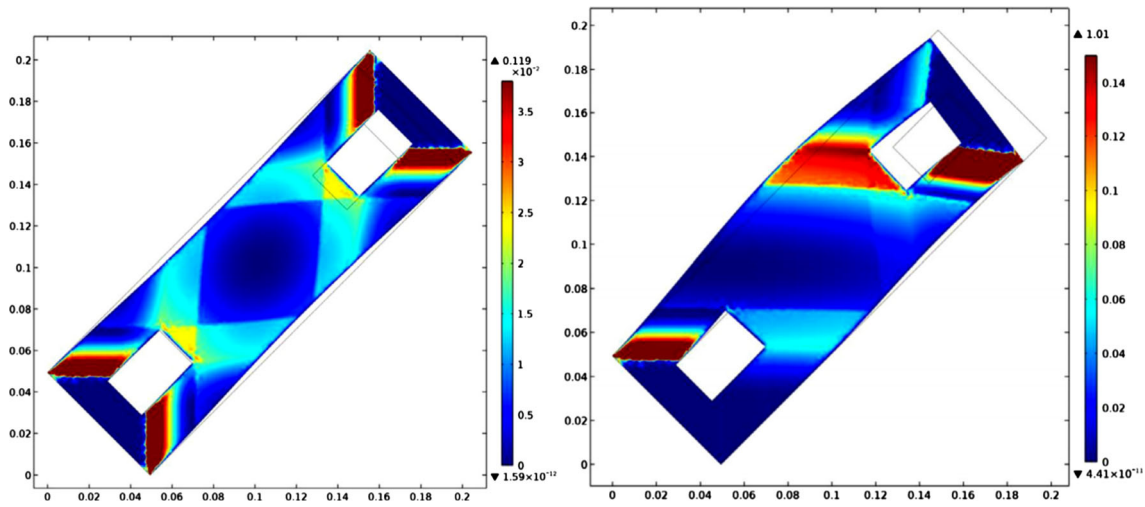


Fig. 16 Color maps of the strain energy density for standard bias extension test (left) and combined rotation-compression test (right) of rectangular linear elastic specimen pantographic fabrics with rectangular holes (color figure online)

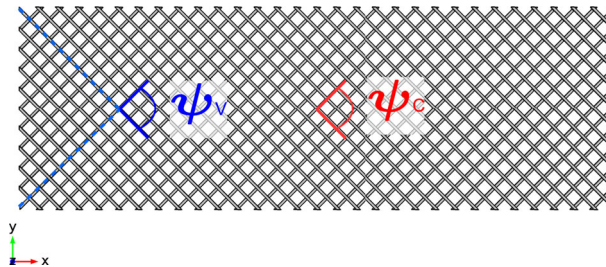


Fig. 17 Two control angles employed in the identification procedure

energy density is coercive and positive definite in such energy space; (3) the set of placements for which the strain energy is vanishing (the so-called floppy modes) must strictly include rigid motions; (4) the restrictions on displacement boundary conditions that ensure the existence and uniqueness of linear static problems are determined.

1.5 Numerical identification of homogenized model

In Ref. [42], the parameters \mathbb{K}_a^α , \mathbb{K}_b^α and \mathbb{K}_p appearing in the strain energy are assumed to be independent of the position and family of beams they are related to and the strain energy density of the homogenized model (18). The parameter identification is numerical, which means that the constitutive parameters \mathbb{K}_e , \mathbb{K}_b and \mathbb{K}_p of the homogenized model are calibrated by means of several numerical computations performed with the 3D Cauchy model of isotropic and homogeneous elastic materials undergoing arbitrarily large strains. Several bias extension test simulations [45] using both the standard Cauchy model and the higher gradient model, for several displacements prescribed on the shorter side of the specimen, are performed. For each simulation, the overall stored energy and two representative deformations at specific points are evaluated. The two representative deformations are chosen to be the angles ψ_C and ψ_V , evaluated at the probed points shown in Fig. 17, i.e., at the center C of the specimen and at the corner V of the “quasi-rigid” triangle near a base of the specimen.

The material parameters of the macromodel \mathbb{K}_e , \mathbb{K}_b and \mathbb{K}_p are estimated by minimizing the squared errors for the overall stored energy and the two angles ψ_C , ψ_V , when computed with both the homogenized and Cauchy models. The two angles ψ_C , ψ_V have been chosen among other possible control quantities because each of them is strongly related to one of the last two energy terms (18) only dependent only on one parameter each. The energy involved in the distortion angle at the center is mostly governed by the parameter \mathbb{K}_p , while the distortion angle at the triangle vertex depends for the most part on the bending energy related to \mathbb{K}_b , thus allowing to easily find the minimum of the squared error for the two angles by separately tuning \mathbb{K}_e and \mathbb{K}_b . The

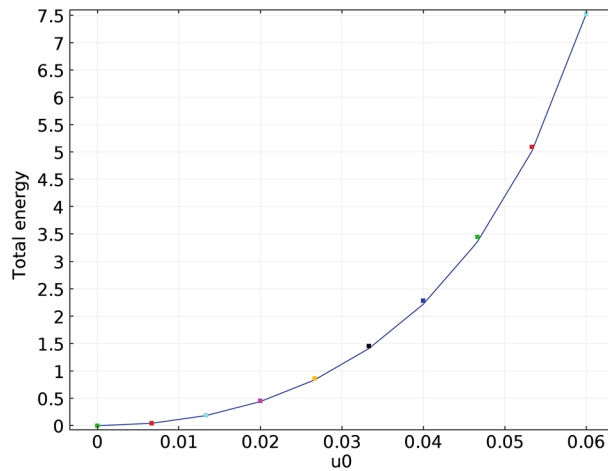


Fig. 18 Comparison of the total energy between the Cauchy model (points) and the second gradient model (solid line)

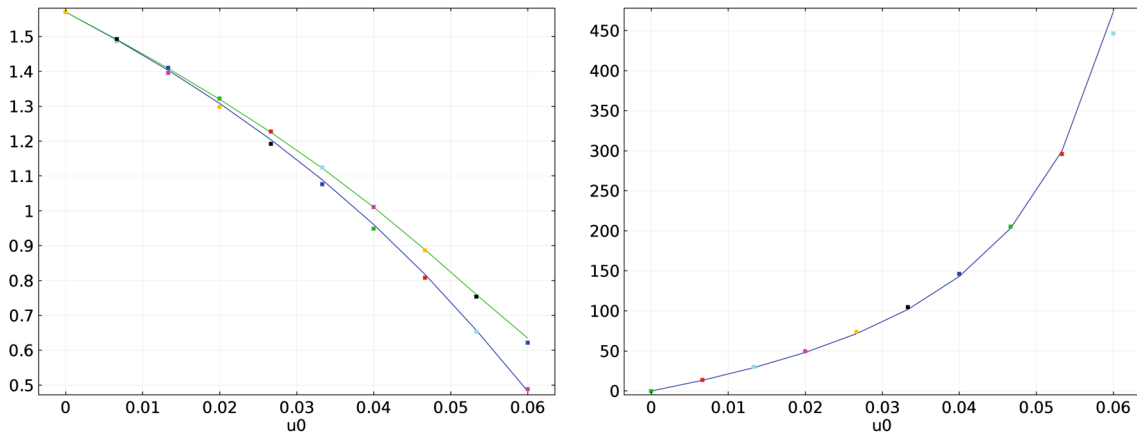


Fig. 19 Comparisons between the Cauchy model (points) and the regression with the second gradient model (solid line). **a** Angle at the center ψ_C (blue line) and angle at the corner ψ_V (green line) on the left; **b** total reaction force (color figure online)

last parameter \mathbb{K}_e is derived by considering the whole stored energy. In Figs. 18 and 19 (left), the total energy and the angles ψ_C and ψ_V used for fitting the second gradient model are shown as the prescribed displacement in the bias extension test is varying. In Fig. 19 (right), a comparison between the total reaction force of the micromodel and the one evaluated with the macromodel is plotted versus the prescribed displacement. This quantity was computed by means of Castigliano's first theorem. Figure 20 shows that for the Cauchy model a non-negligible amount of energy is stored for configurations that are not accounted for in the coarser second gradient model. The main reason is that the Cauchy model has a richer kinematics than the homogenized one. Figure 19 (right) confirms this statement that at large displacements, which are likely to be those where strain energies due to the richer kinematics of the refined model start to gain significance.

1.6 Elastic surface models

In Ref. [46], the formulation of a model for pantographic sheets, which is regarded as elastic surfaces embedded in a three-dimensional Euclidean space, has been first presented. In order to account for the geodesic (thus generalizing the classical plate theory) and out-of-plane bending of fibers, the model exhibits an associated second gradient areal strain energy density, which depends on the first and second gradients of the deformation. Accounting for the fact that fibers are arranged in two material directions, a Lagrangian Cartesian orthonormal coordinate system, whose associated basis of unit vectors is (D_1, D_2) , is introduced in the reference config-

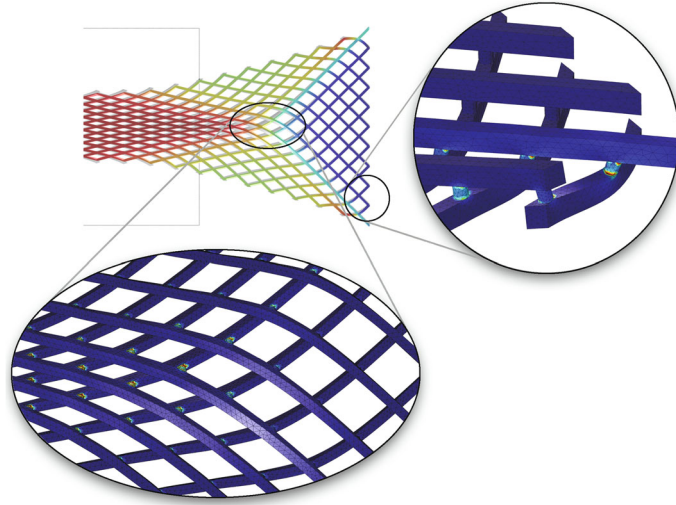


Fig. 20 3D deformation details; the colors in the zooms indicate qualitatively the stored elastic energy density for the 3D Cauchy model (color figure online)

uration. We now consider a 2D continuum, whose reference shape is the rectangular domain $\mathcal{B} \subset \mathbb{R}^2$. As customary, D_1 and D_2 are defined as the push-forward vectors in the current configuration of the vectors D_1 and D_2 , respectively, i.e., $D_\alpha = F D_\alpha$, $\alpha = 1, 2$. In the sequel fiber, stretches $\|D_\alpha\|$ are denoted as λ and μ

$$F = D_1 \otimes D_1 + D_2 \otimes D_2 = \lambda \tilde{D}_1 \otimes D_1 + \mu \tilde{D}_2 \otimes D_2 \quad (19)$$

where $\tilde{D}_\alpha = \frac{D_\alpha}{\|D_\alpha\|}$ are the unit vectors associated with D_α . Such vectors are used to define the fiber shear strain γ as $\sin \gamma = \tilde{D}_1 \cdot \tilde{D}_2$ [13,46]. The shear strain introduced in this model is different from that defined in the Pipkin continuum model [10,34,35]. From Eq. (19), the right Cauchy-Green tensor reads

$$C = F^T F = \lambda^2 D_1 \otimes D_1 + \mu^2 D_2 \otimes D_2 + \lambda \mu \sin \gamma (D_1 \otimes D_2 + D_2 \otimes D_1). \quad (20)$$

and

$$Jn = F D_1 \times F D_2 = D_1 \times D_2 \quad (21)$$

with n the unit normal of the deformed surface field and $J = \lambda \mu |\cos \gamma|$ the local areal dilation due to the deformation. In Ref. [46], the following representation formula is proven

$$\nabla \nabla \chi = (g_1 + K_1 n) \otimes D_1 \otimes D_1 + (g_2 + K_2 n) \otimes D_2 \otimes D_2 + (\Gamma + T n) \otimes (D_1 \otimes D_2 + D_2 \otimes D_1) \quad (22)$$

with

$$g_1 = \lambda \eta_1 p + (D_1 \cdot \nabla \lambda) \tilde{D}_1; \quad g_2 = \mu \eta_2 q + (D_2 \cdot \nabla \mu) \tilde{D}_2 \quad (23)$$

$$\Gamma = (D_1 \cdot \nabla \mu) \tilde{D}_2 + \lambda \mu \phi_1 q = (D_2 \cdot \nabla \lambda) \tilde{D}_1 + \lambda \mu \phi_2 p \quad (24)$$

$$q = n \times \tilde{D}_2; \quad p = n \times \tilde{D}_1 \quad (25)$$

$$K_1 = \lambda^2 \kappa_1; \quad K_2 = \mu^2 \kappa_2; \quad T = \lambda \mu \tau. \quad (26)$$

where η_1 and η_2 are the geodesic curvatures of the deformed fibers, ϕ_1 and ϕ_2 the so-called Tchebychev curvatures, κ_1 and κ_2 the normal curvatures of the deformed fibers, and τ measures the twist of the deformed surface. In Ref. [46], explicit expressions for geodesic and Tchebychev curvatures are provided

$$J \eta_1 = D_1 \cdot \nabla (\mu \sin \gamma) - D_2 \cdot \nabla \lambda$$

$$J \eta_2 = D_1 \cdot \nabla (\mu) - D_2 \cdot \nabla (\lambda \sin \gamma)$$

$$J \phi_1 = J \eta_2 + \lambda D_2 \cdot \nabla (\sin \gamma)$$

$$J \phi_2 = J \eta_1 + \mu D_1 \cdot \nabla (\sin \gamma).$$